JOURNAL OF SYNCHROTRON RADIATION

ISSN 1600-5775

Received 18 October 2018
Accepted 23 May 2019

Edited by I. Schlichting, Max Planck Institute for Medical Research, Germany

[1] This article will form part of a virtual special issue on X-ray free-electron lasers.

Keywords: X-ray free electron lasers; X-ray near-edge spectroscopy; extended X-ray absorption fine structure; X-ray absorption spectroscopy.

XANES and EXAFS of dilute solutions of transition metals at XFELs[1]

Ruchira Chatterjee,[a] Clemens Weninger,[b] Anton Loukianov,[b] Sheraz Gul,[a] Franklin D. Fuller,[a,b] Mun Hon Cheah,[c] Thomas Fransson,[d] Cindy C. Pham,[a] Silke Nelson,[b] Sanghoon Song,[b] Alexander Britz,[b] Johannes Messinger,[e,c] Uwe Bergmann,[d] Roberto Alonso-Mori,[b] Vittal K. Yachandra,[a]* Jan Kern[a]* and Junko Yano[a]*

[a]Molecular Biophysics and Integrated Bioimaging Division, Lawrence Berkeley National Laboratory, 1 Cyclotron Road, Berkeley, CA 94704, USA, [b]LCLS, SLAC National Accelerator Laboratory, Menlo Park, CA 94025, USA, [c]Department of Chemistry – Ångström Laboratory, Molecular Biomimetics, Uppsala University, SE 75237 Uppsala, Sweden, [d]Stanford PULSE Institute, SLAC National Accelerator Laboratory, Menlo Park, CA 94025, USA, and [e]Institutionen för Kemi, Kemiskt Biologiskt Centrum, Umeå Universitet, SE 90187 Umeå, Sweden. *Correspondence e-mail: vkyachandra@lbl.gov, jfkern@lbl.gov, jyano@lbl.gov

This work has demonstrated that X-ray absorption spectroscopy (XAS), both Mn XANES and EXAFS, of solutions with millimolar concentrations of metal is possible using the femtosecond X-ray pulses from XFELs. Mn XAS data were collected using two different sample delivery methods, a Rayleigh jet and a drop-on-demand setup, with varying concentrations of Mn. Here, a new method for normalization of XAS spectra based on solvent scattering that is compatible with data collection from a highly variable pulsed source is described. The measured XANES and EXAFS spectra of such dilute solution samples are in good agreement with data collected at synchrotron sources using traditional scanning protocols. The procedures described here will enable XFEL-based XAS on dilute biological samples, especially metalloproteins, with low sample consumption. Details of the experimental setup and data analysis methods used in this XANES and EXAFS study are presented. This method will also benefit XAS performed at high-repetition-rate XFELs such as the European XFEL, LCLS-II and LCLS-II-HE.

1. Introduction

X-ray absorption spectroscopy (XAS) is a powerful tool for characterizing the local structure of materials (Rehr & Albers, 2000; Smolentsev & Soldatov, 2006; Bunker, 2010). It has two notable advantages: the first is its applicability to gaseous, liquid or solid forms of matter regardless of whether it has long-range order or not; the second advantage is element specificity. Each element has a set of unique X-ray absorption edges, so the local structure around the target element can be analyzed by XAS measurements around its absorption-edge energy. The total absorption region includes X-ray near-edge spectroscopy (XANES) and extended X-ray absorption fine structure (EXAFS). EXAFS records the modulation of an X-ray absorption spectrum in the energy region from 50 eV to approximately 500 eV above the absorption edge (Fig. 1). From the EXAFS analysis, it is possible to extract the number, type and, especially, the distances of the atoms that surround the probed metal center with a high degree of accuracy, and it has been proven to be one of the best tools for investigating local atomic order (Bunker, 2010). On the other hand, XANES focuses on the lower-energy region, starting from

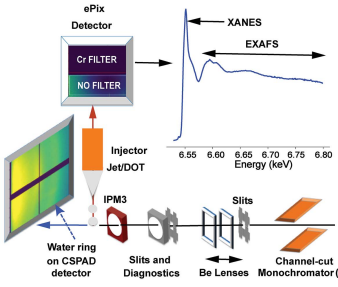

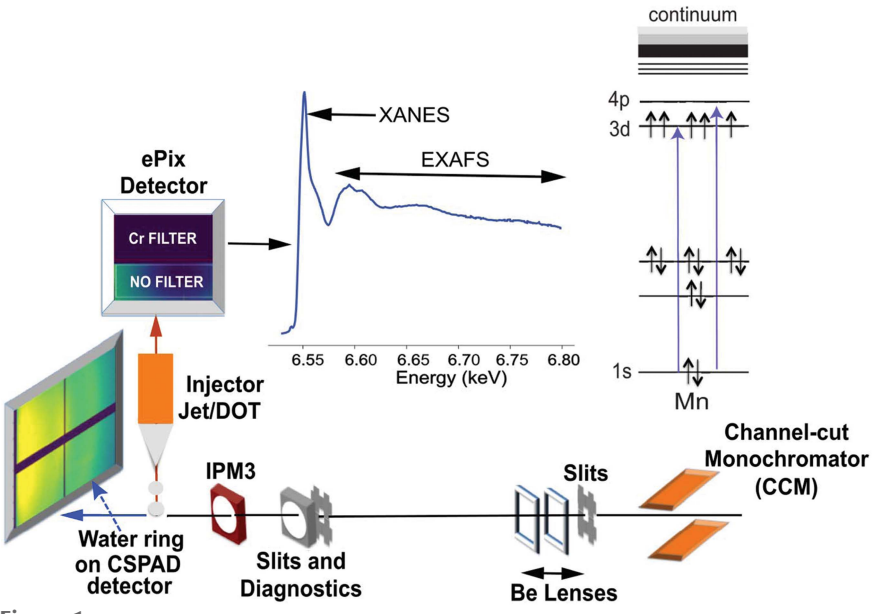

Figure 1
Experimental setup at the XPP station at LCLS for Mn XAS measurements using femtosecond X-ray pulses from the XFEL. (Top) Energy ranges for the XANES and EXAFS regions are illustrated and the probed transition for 3*d* transition metal *K*-edge spectroscopy is shown for Mn as an example. (Bottom) Positions of the monochromator (CCM) and the beam intensity monitor (IPM3) along the beamline, and the positions of the two detectors with respect to the interaction point are indicated.

below the edge and up to approximately 50 eV above the edge. It provides information on the symmetry and electronic structure of the absorbing atom and ligands, as well as the effective charge of the metal. Advanced fitting algorithms have made it possible to determine some structural information also from XANES spectra such as bond lengths and bond angles (Benfatto & Della Longa, 2001; Smolentsev & Soldatov, 2006; Sarangi *et al.*, 2008; Jacquamet *et al.*, 2009), although this comes with the caveat that a sufficiently accurate initial structural model is an essential starting point.

Synchrotron radiation sources have been extensively used over the past several decades to collect XANES and EXAFS spectra on numerous systems in the fields of chemistry, materials science, biology and others. The more common applications have been in the use of steady-state spectroscopy, but there are also time-resolved XANES and EXAFS studies that follow phenomena in time scales of several tens of picoseconds and above (Shelby *et al.*, 2014; Chergui, 2015, 2018). However, there are only a few time-resolved studies that involve dilute solutions, especially for biological systems (Chen *et al.*, 2014).

One of the challenges of conducting time-resolved experiments for biological samples at synchrotron facilities is the fast X-ray induced radiation damage at room temperature caused by the diffusion of solvated electrons and radicals. This is particularly problematic for systems containing redox-active metals, which make up a large fraction of the most interesting biological systems. Such experiments require fast sample replacement to reduce the effects of damage, thus requiring large amounts of samples preferably at high concentrations to obtain good signal-to-noise in the X-ray spectra. However, it is usually difficult to prepare concentrated proteins or other biological samples in the m*M* range, with large volumes in the tens of millilitres or more.

The advent of X-ray free-electron lasers (XFELs) producing ultrashort intense X-ray pulses (pulse widths < 100 fs) has enabled experiments in the sub-picosecond time-scale in an increasing number of scientific fields such as chemistry (Bressler *et al.*, 2009), solid-state physics (Kachel *et al.*, 2009) and plasma physics (Levy *et al.*, 2012; Abela *et al.*, 2017). The use of femtosecond X-ray pulses has made it possible to outrun radiation damage caused by diffusion processes and collect data before the sample is destroyed at room temperature (Alonso-Mori *et al.*, 2012). Moreover, the significantly faster time resolution and increased peak brilliance (several order of magnitude higher) per pulse compared with synchrotrons make XFELs a unique resource for time-resolved X-ray spectroscopic techniques. This makes time-resolved experiments on dilute samples such as femtosecond-scale XAS and resonant inelastic X-ray scattering (RIXS) studies at room temperature a particularly attractive class of experiments using XFELs. These experiments can be performed with reasonable data acquisition times and the latter class of experiments can only be carried out at XFELs. It should be noted that other modifying processes may happen to the samples with highly focused (extremely brilliant, nm focus) XFEL pulses, but these are not usually a problem under typical XFEL experimental conditions (down to few µm focus) (Alonso-Mori *et al.*, 2012), especially for XAS experiments in which the insertion of a monochromator significantly reduces the X-ray flux.

At XFELs, X-ray emission spectroscopy (XES) is used more frequently than XAS (Alonso-Mori *et al.*, 2015). This is, in part, because SASE (self-amplified spontaneous emission) pink beam can be used for the XES data collection where the incoming energy is kept constant without monochromatizing the beam. This is also complementary with forward-scattering techniques (X-ray diffuse scattering and X-ray diffraction). On the other hand, in the case of XAS, the use of a monochromator reduces the incoming X-ray photons down to 1%, strongly limiting the photon levels for XAS. In addition, some of the challenges of XAS for dilute biological samples include the requirement of (i) running the XFELs in scanning mode over large energy ranges; (ii) normalization of data at each energy point, from a highly variable incident source and from the shot-by-shot fluctuation of the probed sample volume; and (iii) the requirement of a large amount of sample. However, as described above, there is a strong desire to conduct XAS, particularly EXAFS, at XFELs for dilute biological samples similar to the way it is used at synchrotron facilities. There are

efforts in progress to make XANES and EXAFS the methods of choice for XFEL metalloenzyme studies. XANES has already been demonstrated at XFELs for metalloproteins like cytochrome *c* and myoglobin (Levantino *et al.*, 2015; Mara *et al.*, 2017; Miller *et al.*, 2017), showing protein conformational changes. All these studies were performed using a Rayleigh jet for sample delivery. In this study, we address each of the above three issues and show that one can obtain both XANES and EXAFS spectra from dilute solution samples using two sample delivery systems, the Rayleigh jet and drop-on-demand setup.

2. Methods

X-ray absorption (XANES and EXAFS) measurements at the Mn *K*-edge were performed at the X-ray pump and probe (XPP) endstation of the Linac Coherent Light Source (LCLS) (Chollet *et al.*, 2015). The X-ray beam had a pulse length of ∼40 fs and a pulse energy of 2.4–3.1 mJ before the monochromator, corresponding to 2×10^{12} to 3×10^{12} photons per pulse, at a repetition rate of 120 Hz. The sample was a solution of 10 m*M* and 50 m*M* manganese chloride hexahydrate ($MnCl_2{\cdot}6H_2O$) (Sigma-Aldrich) in deionized water.

The Si(111) channel-cut monochromator (CCM) of XPP with a resolution of 1.4×10^{-4} $\Delta E/E$ was used to monochromatize the incoming X-ray pulses, yielding about 1% of the SASE photons (∼3×10^{10} photons per pulse) in the monochromatic beam. By changing the CCM, the X-ray energy at the XFEL was scanned in a stepwise manner. To assure roughly equal photon numbers at each energy point over the scan range, the monochromator energy setting was followed by the machine configuration. This involved automatic tuning of the central energy of the LCLS electron beam to the current CCM setting. To achieve similar focusing quality over the entire range from 6530 eV to 6800 eV, a set of three compound beryllium refractive lenses (thicknesses of 100 µm, 200 µm and 500 µm) was used and automatically translated longitudinally along with the energy during the energy scan to keep the focus spot size constant at around 5 µm full width at half-maximum (FWHM) while changing the energy. Beam intensity was recorded for each shot after the monochromator using one of the XPP I_0 intensity position monitors (IPM3) that measures the intensity of X-rays scattered from a thin foil inserted into the beam. The scan protocol for the spectra measured on the Rayleigh jet used a step size of 1 eV in the range from 6530 eV to 6540 eV and a step size of 0.5 eV from 6540.5 eV to 6579 eV with an exposure time for 240 shots (2 s) at each energy position. For the EXAFS region from 6579 eV up to 6800 eV, the step size was increased gradually from 0.6 eV to 3 eV. The exposure times were increased with higher energies; 2 s for 6579 eV to 6702 eV, 4 s for 6705 eV to 6766 eV and 6 s for 6769 eV to 6800 eV. The energy ramp procedure employed required 4 s for establishing each new energy position, leading to a total measurement time of at least 6 s for each energy point. For the XANES scans on the single droplets using the drop-on-demand setup, a step size of 1 eV was used for the ranges 6535 eV to 6545 eV and 6559 eV to 6570 eV and a step size of 0.5 eV for the range from 6545 eV to 6559 eV with an exposure time of 8 s (= 960 shots) per energy point.

Mn XAS spectra were recorded as fluorescence excitation spectra using an ePix-100 detector with 768 pixels × 704 pixels (Blaj *et al.*, 2015) mounted facing the interaction region at an angle of 90° with respect to the beam to minimize the amount of elastic scattering (Fig. 1). The distance between the interaction region and the detector surface was ∼15 mm. The detector active area is about 38 mm × 35 mm, covering a solid angle of ∼0.14 sterad. A chromium foil was placed in front of half of the detector, yielding a solid angle of 0.07 sterad for each of the filtered and unfiltered fluorescence data collection. The water scattering intensity was collected in the forward-scattering geometry using a CSPAD 140k 2D pixel array detector (388 pixels × 370 pixels; Herrmann *et al.*, 2013; Blaj *et al.*, 2015) placed ∼20 mm off center at *ca*. 130 mm downstream of the X-ray intersection point with the sample (Fig. 1). This scattering signal was used for normalization (see Fig. 4), which will be shown to be vital if the sample path length varies on a shot-by-shot basis.

The solution sample was delivered by two different methods: for liquid jet delivery, a capillary with an inner diameter of 500 µm was used and the samples were pumped through the capillary at a flow rate of 15 ml min^{-1} using an HPLC pump. After the interaction point, the solution was caught by a catcher and recirculated. For drop-on-demand sample delivery, the 'drop on tape' (DOT) with acoustic droplet ejection setup previously described (Fuller *et al.*, 2017) was used with a droplet diameter of ∼200 µm at a flow rate of 40 µL min^{-1} and a drop deposition frequency of 120 Hz in sync with the LCLS. Both setups were mounted inside a helium enclosure installed at the XPP endstation, having the entire beam path upstream of the sample as well as the signal path between the interaction point and the fluorescence detector under a helium atmosphere. The time required for the XAS measurements using the two methods are discussed in a later section (see also Table 1).

Data reduction of XAS spectra was performed using *SamView* (*SixPack* software, available at http://www.sams-xrays.com/sixpack). The program *Athena* of the *Demeter* software package (Ravel & Newville, 2005) was used to align XAS data and subtract the pre-edge and post-edge backgrounds. The spectra were then normalized to the edge jump. A five-domain cubic spline was used to remove the low-frequency background in *k*-space and the resulting *k*-space data, $k^3\chi(k)$, was then Fourier transformed (FT) into *r*-space.

2.1. XAS from synchrotron

Mn *K*-edge X-ray absorption data were collected using beamline 7-3 at Stanford Synchrotron Radiation Laboratory (SSRL), operating with standard ring conditions of 3.0 GeV energy and 500 mA current. The intensities of incident and transmitted X-rays were monitored with N_2-filled ion chambers before (I_0) and after the sample (I_1 and I_2), respectively.

Table 1
Comparison of the sample delivery methods and experimental parameters.

		Rayleigh jet	DOT
Parameters of Rayleigh jet and DOT			
X-ray hit rate		100	∼80
Path length (µm)		500	200
Flow rate (min^{-1})		15 ml	40 µl
Probed volume ($\times 10^3$ µm^3) per shot		∼10	∼4
Average counts per shot†		1400	450
Comparison of data collection time‡			
X-ray rep. rate 120 Hz	Data collection time	35 min	120 min
	Total sample volume	525 ml	5 ml
X-ray rep. rate 360 Hz§	Data collection time	∼12 min	40 min
	Total sample volume	175 ml	5 ml¶
kHz XFEL experiments using gas dynamic virtual nozzle jets††			
X-ray rep. rate 27 000‡‡	Data collection time	∼80 min	
	Total sample volume	3 ml	

† At the edge jump for 10 m*M* Mn solution. ‡ The data collection time and total sample volume required to reach 1 000 000 counts for the edge jump for 10 m*M* Mn concentration using a 5 µm-diameter beam size; energy range calculated for EXAFS: 6530–6800 eV; number of points: 202. § The frequency expected for the hard X-rays at LCLS-II-HE. ¶ Flow rate for DOT at 360 Hz: 120 µl min^{-1}. †† Flow rate: 40–50 µl min^{-1}; path length: 4 µm; pulse power: 0.5 mJ (Grünbein *et al.*, 2018; Wiedorn *et al.*, 2018). Due to the shorter path length, the estimated time for the measurement is longer than the Rayleigh jet. ‡‡ Effective number of X-ray shots per second at the EuXFEL (2700 shots per pulse train, 10 pulse trains per second) where the signal will be averaged over the number of shots.

A solution sample of 50 m*M* $MnCl_2$ in 50% glycerol (*w*/*v*) was loaded in 40 µl plexiglass sample holders having a Mylar tape window on one side, and frozen immediately in liquid nitrogen. XAS data of samples were collected as fluorescence excitation spectra using a 30-element Ge solid-state detector (Canberra). The monochromator energy was calibrated with the pre-edge peak of $KMnO_4$ (6543.3 eV). To control and minimize the X-ray damage, data were collected at 10 K using a liquid-He flow cryostat (Oxford Instruments).

3. Results

3.1. XAS data collection at LCLS

The most common way to perform XAS experiments is to select the incoming radiation wavelength using a crystal monochromator and scan the wavelength. At XFELs, the typical SASE bandwidth is 30–40 eV at 6600 eV, with significant intensity and wavelength fluctuations on a shot-by-shot basis. Therefore, each energy point (after monochromatization) of the XAS spectrum is obtained by averaging over a number of shots (Lemke *et al.*, 2013) to achieve a reasonable signal-to-noise ratio. Seeded beam has been demonstrated in both hard X-ray (Amann *et al.*, 2012) and soft X-ray operation (Ratner *et al.*, 2015) at LCLS and it has been applied for XAS measurements without a monochromator in the soft X-ray region (Kroll *et al.*, 2016). Although the band width for hard X-rays (0.4–1 eV) of the seeded beam would potentially be useable for XAS scans, it is predominantly used with the low charge operation mode at LCLS in the hard X-ray regime, thus giving a smaller total number of photons (Amann *et al.*, 2012). Therefore, the expected gain in photon numbers when using the monochromator in combination with seeded beam instead of an SASE beam is only modest, and it is often offset by the additional time requirements for machine tuning. For these reasons, we opted to use a monochromator and adjusted the central energy of the electron beam during the energy scan to keep the center of the SASE bandwidth at the energy given by the current monochromator setting. In addition, the scan script included an adjustment of the position of the focusing lenses to ensure a uniform focus spot size over the entire XANES and EXAFS scan ranges employed here.

Fig. 2(*a*) shows the EXAFS of 50 m*M* $MnCl_2$ solution, collected by monitoring the changes in the fluorescence signal as a function of incident X-ray energy. The sample was flowed using an HPLC pump through a 500 µm-diameter cylindrical

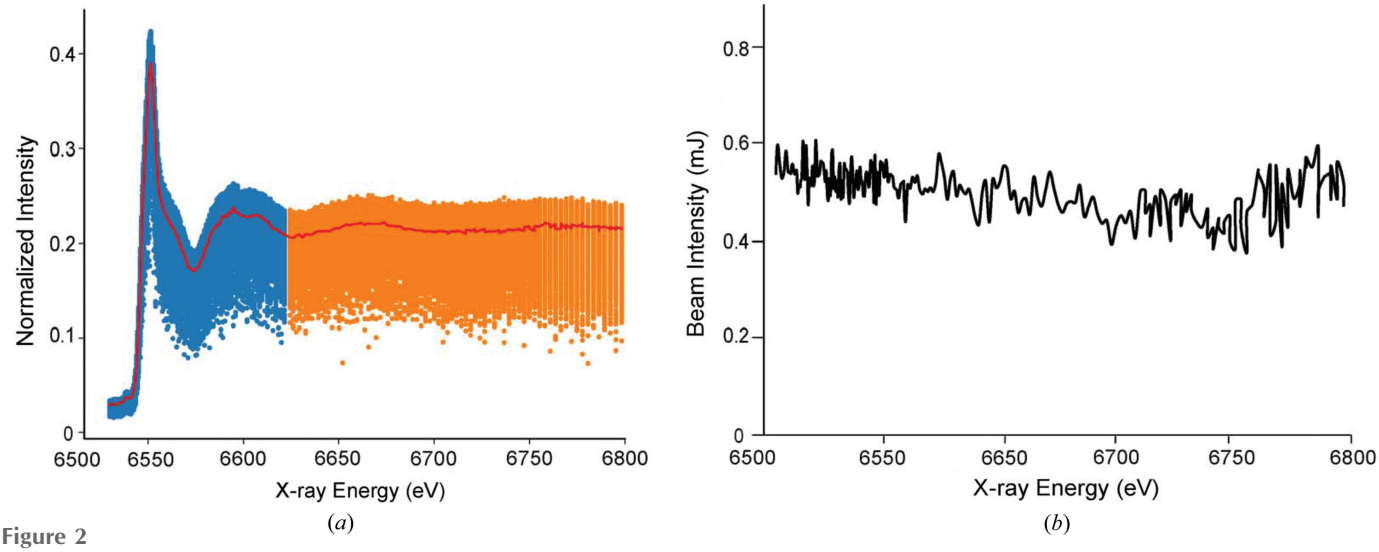

Figure 2
(*a*) XAS data collected for each shot (dots) normalized to the incoming X-ray (I_0) from IPM3 (scatter plot) where pre-edge and edge regions, from 6530 eV to 6621.5 eV, are shown in blue and the shape resonance, from 6623 eV to 6798.3 eV, is shown in orange. The red line is the mean of the data for each energy point. (*b*) Incoming X-ray (I_0) intensity measured at IPM3 after the monochromator as a function of the X-ray energy. By adjusting the central energy of the FEL during the energy scan, the beam intensity after the monochromator was kept roughly constant.

liquid jet oriented perpendicular with respect to the incoming X-ray beam. We observed that the incoming X-ray intensity (I_0) measured with the intensity position monitor after the monochromator (IPM3) is relatively stable with respect to the change in X-ray energy by moving the CCM [Fig. 2(*b*)].

The XAS spectrum was collected in fluorescence mode. Each image was pre-processed by subtracting a previously collected background using a dark run. For each shot, each pixel of the background-subtracted image was clipped by a threshold value such that the zero-photon peak in the image histogram was removed. Finally, the signal on the pixels in the region of interest was summed to give the integrated signal. The integrated counts for each shot are divided by the value recorded by IPM3 for each shot and are grouped according to the monochromator scan position [Fig. 2(*a*), scatter plot]. The IPM3 values were filtered to select the central 90% of values, similar to the outlier rejection previously applied in other studies (Lemke *et al.*, 2013). The remaining values are averaged within the group to produce a mean value [Fig. 2(*a*), red line], representing the final I_0 normalized XAS data.

This approach is similar to that described previously for data collection using a liquid jet (*e.g.* Lemke *et al.*, 2013; Shelby *et al.*, 2016; Mara *et al.*, 2017). We note that this normalization procedure requires a stable running jet, and often samples might not be available in sufficient quantities for operation of a Rayleigh jet. Sample consumption can be minimized by the use of an electrospinning jet (Sierra *et al.*, 2012, 2016), but these jets only offer a very short path length of <10 µm, limiting the sample volume that can be probed per shot. Also, electrospinning jets require additives like glycerol that may not be compatible with all types of samples. An alternative approach is to use a drop-on-demand system where drops of the desired diameter are brought into the X-ray interaction point at the right time for each individual X-ray shot but no sample is running at the time between X-ray shots. Thus a large X-ray pathlength (200–300 µm) close to the attenuation length of the solvent (540 µm for water at 6600 eV) can be achieved, while requiring only modest sample volumes and being compatible with a wide range of buffer conditions. The drawback of such an approach is that the droplet position varies slightly from shot to shot, leading to variations in the volume probed by each X-ray shot and requiring a robust normalization procedure that takes this into account. Later in the paper, we will discuss the application of such a drop-on-demand setup for XAS in the section describing the normalization procedures.

3.2. Effect of filters

Although the ePix detector provides some energy resolution, it is not sufficient to distinguish scattered photons at the incoming energy reliably from the signal fluorescence photons. For the XAS data collection of dilute samples at synchrotron facilities, thin $Z-1$ filters are often used for reducing scattering signals reaching the fluorescence detector. We have tested this effect by covering one half of the ePix detector with a 10 µm chromium foil using the liquid jet setup. This setup allows collection of Mn EXAFS data with and without a filter simultaneously from the same samples (Fig. 3). Although a small reduction in noise levels is visible in the pre-edge region due to the filter and the calculated signal-to-noise ratio for the edge jump is higher when using a filter, no significant positive effects of the filter on the quality of the spectra were observed under the conditions of the present experimental setup (Fig. 3). This implies that the scatter is not significant and also most of the scatter is from the sample, and there is little scattering from other scattering sources in this configuration because of the small beam size (~5 µm diameter) compared with the diameter of the jet (~500 µm).

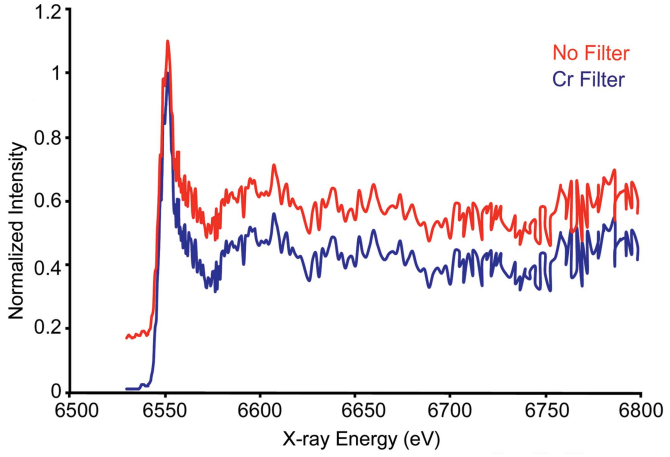

Figure 3
Raw data, without normalization protocols applied, for the EXAFS spectrum collected using a jet with (blue) and without (red) a Cr filter. The spectra are normalized to the edge height and the 'No filter' spectrum is vertically offset. The numbers of shots used for different energy ranges are as follows: (i) 2400 shots for 6530–6540 eV (2 s × 120 s^{-1} × 10 energy points, step size 1eV), (ii) 18480 shots for 6540.5–6579eV (2 s × 120 s^{-1} × 77 energy points, step size 0.5eV), (iii) 18720 shots for 6579–6702 eV (2 s × 120 s^{-1} × 78 energy points, step size 1.5 eV), (iv) 12000 shots for 6705–6766 eV (4 s × 120 s^{-1} × 25 energy points, step size 2.4 eV) and (v) 8640 shots for 6769–6800 eV (6 s × 120 s^{-1} × 12 energy points, step size 3 eV).

3.3. XAS normalization

For the XAS data collection, accurate measurement of the absorption coefficient changes as a function of the excitation energy is critical. In particular, weak EXAFS oscillations of dilute protein samples that are typically less than 10% of the *K*-edge jump need to be accurately captured over a ~500 eV scan range. At XFELs, one needs to consider two types of fluctuation that do not exist in synchrotron-based data collection. The first is the shot-by-shot pulse intensity fluctuation of the SASE beam that can be up to 100%. The second is a shot-by-shot change of the probed sample. The shot-by-shot sample replacement requires liquid jets, rastering of a solid target or drop-on-demand sample delivery methods. For the highly stable Rayleigh jet with a fast flow rate (15 ml min^{-1}), as used in the collection of the data presented in Fig. 3, normalization by the incoming beam intensity measured by the IPM3 I_0 monitor was sufficient. To allow data collection using other sample delivery methods that are more

prone to fluctuations in sample volume in the interaction region, it is beneficial to establish a normalization method that accounts for the fluctuation of the probed volume in addition to the I_0 fluctuation.

In Fig. 4, we show the effect of two normalization methods, one using I_0 (incoming X-ray intensity) and the other using the solvent scattering collected on a downstream detector simultaneously with the fluorescence signal. The measurements were conducted using a 50 m*M* $MnCl_2$ solution in a Rayleigh jet (500 µm). The use of solvent scattering for normalization has the advantage that it accounts for both the X-ray pulse energy fluctuations as well as fluctuations of the probed sample volume. Fig. 4(*a*) shows the forward-scattering image on the downstream off-axis CSPAD detector that includes the solvent scattering ('water ring'). The solvent scattering signal is isotropic and generates a broad ring-like feature. The strength of the solvent scattering is determined by radially integrating the counts over the q-range of the water scattering maximum indicated by the white dotted lines in Fig. 4(*a*) and then averaging over all shots for each energy point. These counts are used to normalize the XAS signal. Fig. 4(*c*) shows the EXAFS spectra of the $MnCl_2$ solution with normalization by I_0 or by the water scattering intensity. Both normalization methods give similar k^3-weighted EXAFS and FT spectra [Figs. 4(*b*), 4(*d*) and 4(*e*)], but the signal-to-noise level is better with the water scattering normalization. Overall, the EXAFS spectra taken at the XFEL match well with the synchrotron cryogenic data [Figs. 4(*f*)–4(*h*)].

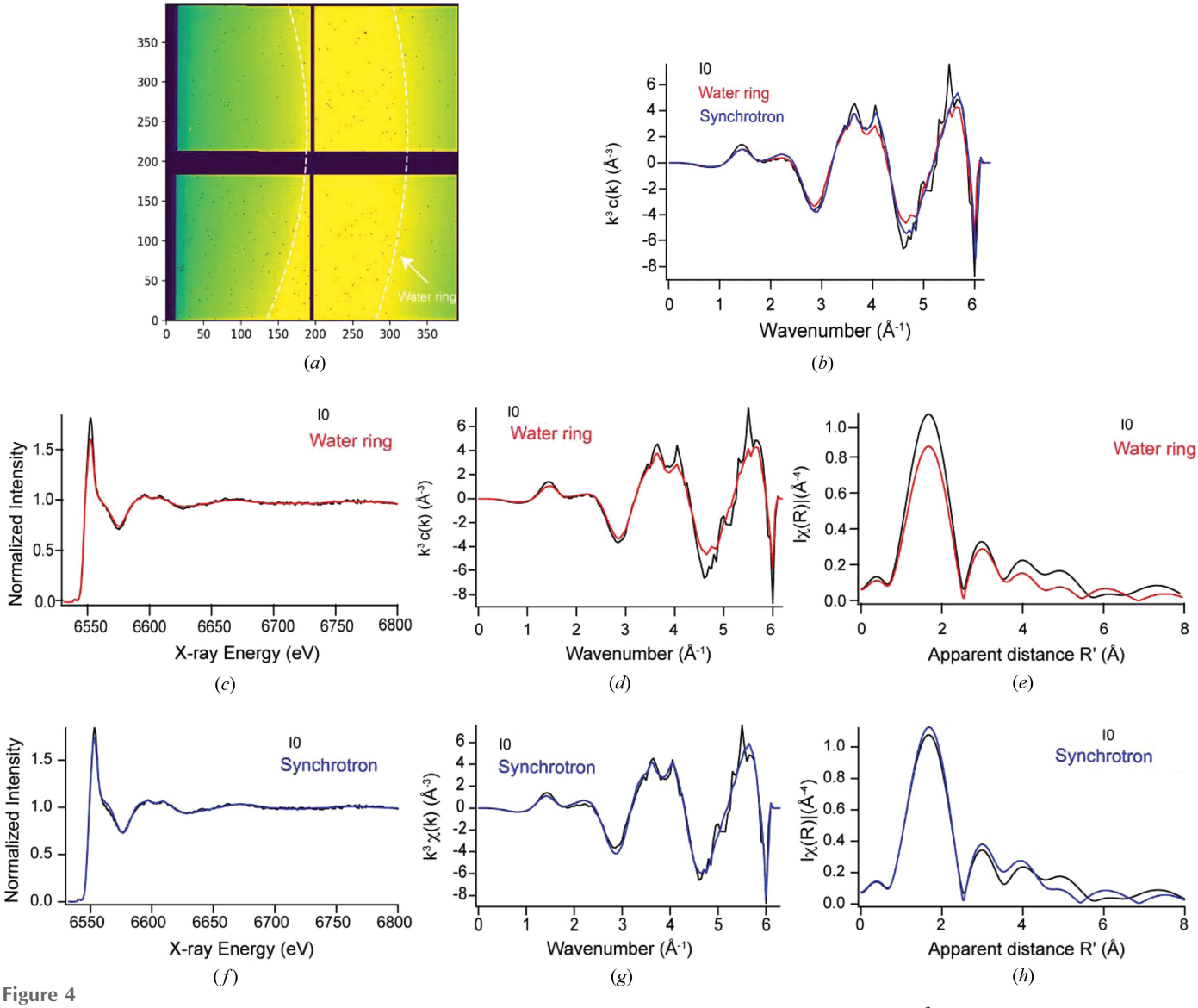

Figure 4
(*a*) Water scatter ring from the jet marked in white collected on a downstream CSPAD used for normalization. (*b*) k^3-Weighted Mn EXAFS spectra of 50 m*M* $MnCl_2$ collected at the synchrotron at cryogenic temperature (blue) and using a jet without a Cr filter normalized using incoming X-rays (I_0) (black) and water scattering intensity (red) at the XFEL. (*c*) Mn EXAFS spectrum collected using a jet without a Cr filter normalized using incoming X-rays (I_0) (black) and water scattering intensity (red), and their (*d*) k^3-weighted EXAFS and (*e*) FT EXAFS spectra. (*f*) Mn EXAFS spectrum collected at the synchrotron at cryogenic temperature (blue) and room temperature with a jet normalized using incoming X-rays (I_0) (black, without Cr filter) at LCLS, and their (*g*) k^3-weighted EXAFS and (*h*) FT EXAFS spectra.

3.4. XAS using different sample delivery methods

A real challenge for the XAS data collection of many biological systems is the need to minimize the required sample volume for data collection, while the Rayleigh jet employed provides a constant probing volume of a path length of 500 µm with a 100% hit rate. Most proteins cannot be obtained in the quantity required for this sample delivery method. In many cases, the reactions of interest in proteins are not easily reversible, and therefore the sample often cannot be brought back to the initial chemical state after triggering the reaction. Hence, recirculation of such samples is not feasible, precluding the use of fast-flowing liquid jets. In order to probe changes in chemical states of such biological samples in time-resolved room-temperature experiments at XFELs, other sample delivery approaches have to be utilized. Recently, we have demonstrated that by using the DOT setup with a path length of ∼200 µm we can follow changes in the chemical states triggered by illumination or gas activation with efficient sample consumption through its application to crystallography and XES methods (Fuller *et al.*, 2017). In the current study, we used the DOT setup for XAS data collection of an $MnCl_2$ (10 m*M*) solution sample to optimize the normalization methods that can be used effectively for dilute biological samples. To take into account the significant changes in both the I_0 and the probed volume due to slightly different positioning of the drop on the tape, the method of normalizing the Mn fluorescence signal using water scattering intensity is critical, particularly for measuring dilute samples. The normalized data using both incoming X-ray (I_0) and the water scatter ring intensity of the Mn XANES spectrum for the DOT setup is shown in Fig. 5. The details of the normalization procedure are the same as described in the previous section. The normalization by the water scattering signal produced better (less noisy) results as shown in Fig. 5(*b*); thus, this method becomes highly important when the probed sample volume changes on a shot-by-shot basis. The total sample volume used to obtain the spectrum in Fig. 5(*b*) was 280 µl with a data collection time of ∼7 min. This contrasts with a consumption of 75 ml that would be necessary to obtain a similar spectrum using a Rayleigh jet due to the unprobed (dead) volume. It should be noted that this comparison is not taking into account the possibility to recirculate the sample as such option might not be feasible in many cases.

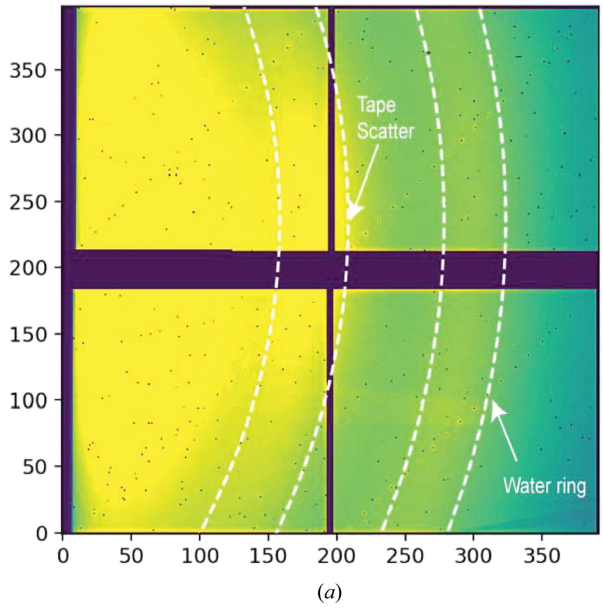

(*a*)

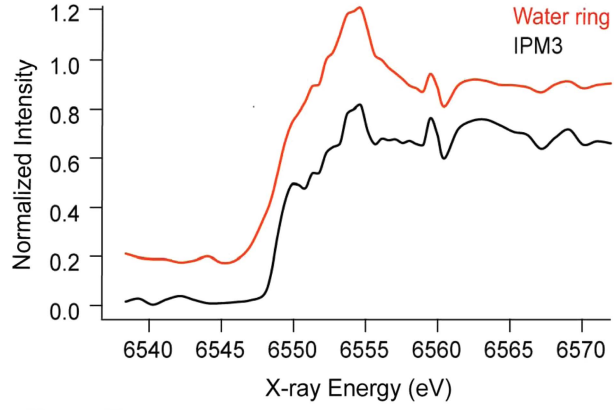

(*b*)

Figure 5
(*a*) Water scatter ring marked in white collected on a downstream CSPAD used for normalization. (*b*) Mn XANES spectrum of a 10 m*M* $MnCl_2$ solution collected using the DOT setup normalized in two different ways, using either the I_0 reading after the monochromator ('IPM3', black), or the integrated scattering intensity in the water ring region on the forward-scattering detector ('Water ring', red). The plots are normalized to 1 and with an offset of 0.2 along the vertical axis. For XANES scans on the single droplets using the DOT setup, the numbers of shots used for different energy ranges are as follows: (i) 9600 shots (8 s × 120 s^{-1} × 10 energy points, step size 1 eV) for 6535–6545 eV, (ii) 26 880 shots (8 s × 120 s^{-1} × 28 energy points, step size 0.5 eV) for 6545–6559 eV and (iii) 10 560 shots (8 s × 120 s^{-1} × 11 energy points, step size 1 eV) for 6559–6570 eV.

4. Conclusions and future directions

We have demonstrated an XAS (XANES + EXAFS) data collection protocol that is suitable at XFEL sources using $MnCl_2$ solution samples at a 50 m*M* concentration delivered by a Rayleigh jet and 10 m*M* concentration delivered using a drop-on-demand setup. The normalization method for the XAS data that uses the water scattering signal described here can be used for dilute systems, compensating for shot-by-shot fluctuations in beam intensity as well as in probed sample volume. In this study we collected EXAFS data up to 300 eV but it is straightforward to extend the scanning range to above 500 eV as required for higher resolved EXAFS (covering *k*-space out to 12 Å^{-1}). The only modification required is that an additional set of focusing lenses needs to be employed, so that a constant focus size can be maintained over the entire scan range. Thus, this experiment lays the foundations for future XAS measurements for dilute proteins at XFELs. In addition to EXAFS, the approach described here will be critical for performing time-consuming RIXS measurements at XFELs that share the same issue of normalizing the data by energy points. From our studies, we estimate at the current LCLS repetition rate of 120 Hz, one can collect a XANES spectrum

in 1–2 h for biological samples with a ∼1 m*M* metal concentration using the DOT setup and EXAFS spectra of ∼1 m*M* metal concentration using a Rayleigh jet in ∼6 h. The data collection time and the sample consumption estimated from the current study are summarized in Table 1. The method of choice will depend on whether the experiment is limited by available sample quantity or data collection time. Experiments will also benefit by the next generation of XFELs, that will feature significantly higher repetition rates like the European XFEL (27 kHz), which recently started user operation (Tschentscher *et al.*, 2017; Grünbein *et al.*, 2018; Wiedorn *et al.*, 2018), LCLS-II (1 MHz) and LCLS-II-HE (360 Hz).

Acknowledgements

The authors would like to thank Isabel Bogacz for her assistance in collecting the synchrotron data.

Funding information

This work was supported by the National Institutes of Health [Grant Nos GM110501(JY), GM126289 (JK) and GM055302 (VKY)], the Director,Office of Science, Office of Basic Energy Sciences (OBES), Division of Chemical Sciences, Geosciences and Biosciences of the Department of Energy (DOE) (contract No. DE-AC02-05CH11231 (JY, VKY), Energimyndigheten and Vetenskapsrådet(2016–05183) (JM), Vetenskapsrådet (2017–00356) (TF) and the Ruth L. Kirschstein NationalResearch Service Award (GM116423-02, FDF). Use ofthe LCLS, SLAC National Accelerator Laboratory, is supported by the US DOE, Office of Science, OBES (Contract No. DE-AC02-76SF00515).

References

Abela, R., Beaud, P., van Bokhoven, J. A., Chergui, M., Feurer, T., Haase, J., Ingold, G., Johnson, S. L., Knopp, G., Lemke, H., Milne, C. J., Pedrini, B., Radi, P., Schertler, G., Standfuss, J., Staub, U. & Patthey, L. (2017). *Struct. Dyn.* **4**, 061602.

Alonso-Mori, R., Kern, J., Gildea, R. J., Sokaras, D., Weng, T. C., Lassalle-Kaiser, B., Tran, R., Hattne, J., Laksmono, H., Hellmich, J., Glöckner, C., Echols, N., Sierra, R. G., Schafer, D. W., Sellberg, J., Kenney, C., Herbst, R., Pines, J., Hart, P., Herrmann, S., Grosse-Kunstleve, R. W., Latimer, M. J., Fry, A. R., Messerschmidt, M. M., Miahnahri, A., Seibert, M. M., Zwart, P. H., White, W. E., Adams, P. D., Bogan, M. J., Boutet, S., Williams, G. J., Zouni, A., Messinger, J., Glatzel, P., Sauter, N. K., Yachandra, V. K., Yano, J. & Bergmann, U. (2012). *Proc. Natl Acad. Sci. USA*, **109**, 19103–19107.

Alonso-Mori, R., Sokaras, D., Zhu, D., Kroll, T., Chollet, M., Feng, Y., Glownia, J. M., Kern, J., Lemke, H. T., Nordlund, D., Robert, A., Sikorski, M., Song, S., Weng, T.-C. & Bergmann, U. (2015). *J. Synchrotron Rad.* **22**, 612–620.

Amann, J., Berg, W., Blank, V., Decker, F. J., Ding, Y., Emma, P., Feng, Y., Frisch, J., Fritz, D., Hastings, J., Huang, Z., Krzywinski, J., Lindberg, R., Loos, H., Lutman, A., Nuhn, H. D., Ratner, D., Rzepiela, J., Shu, D., Shvyd'ko, Y., Spampinati, S., Stoupin, S., Terentyev, S., Trakhtenberg, E., Walz, D., Welch, J., Wu, J., Zholents, A. & Zhu, D. (2012). *Nat. Photon.* **6**, 693–698.

Benfatto, M. & Della Longa, S. (2001). *J. Synchrotron Rad.* **8**, 1087–1094.

Blaj, G., Caragiulo, P., Carini, G., Carron, S., Dragone, A., Freytag, D., Haller, G., Hart, P., Hasi, J., Herbst, R., Herrmann, S., Kenney, C., Markovic, B., Nishimura, K., Osier, S., Pines, J., Reese, B., Segal, J., Tomada, A. & Weaver, M. (2015). *J. Synchrotron Rad.* **22**, 577–583.

Bressler, C., Milne, C., Pham, V. T., Elnahhas, A., van der Veen, R. M., Gawelda, W., Johnson, S., Beaud, P., Grolimund, D., Kaiser, M., Borca, C. N., Ingold, G., Abela, R. & Chergui, M. (2009). *Science*, **323**, 489–492.

Bunker, G. (2010). *Introduction to XAFS: A Practical Guide to X-ray Absorption Fine Structure Spectroscopy*. Cambridge University Press.

Chen, L. X., Zhang, X. & Shelby, M. L. (2014). *Chem. Sci.* **5**, 4136–4152.

Chergui, M. (2015). *Acc. Chem. Res.* **48**, 801–808.

Chergui, M. (2018). *Coord. Chem. Rev.* **372**, 52–65.

Chollet, M., Alonso-Mori, R., Cammarata, M., Damiani, D., Defever, J., Delor, J. T., Feng, Y., Glownia, J. M., Langton, J. B., Nelson, S., Ramsey, K., Robert, A., Sikorski, M., Song, S., Stefanescu, D., Srinivasan, V., Zhu, D., Lemke, H. T. & Fritz, D. M. (2015). *J. Synchrotron Rad.* **22**, 503–507.

Fuller, F. D., Gul, S., Chatterjee, R., Burgie, E. S., Young, I. D., Lebrette, H., Srinivas, V., Brewster, A. S., Michels-Clark, T., Clinger, J. A., Andi, B., Ibrahim, M., Pastor, E., de Lichtenberg, C., Hussein, R., Pollock, C. J., Zhang, M., Stan, C. A., Kroll, T., Fransson, T., Weninger, C., Kubin, M., Aller, P., Lassalle, L., Bräuer, P., Miller, M. D., Amin, M., Koroidov, S., Roessler, C. G., Allaire, M., Sierra, R. G., Docker, P. T., Glownia, J. M., Nelson, S., Koglin, J. E., Zhu, D. L., Chollet, M., Song, S., Lemke, H., Liang, M. N., Sokaras, D., Alonso-Mori, R., Zouni, A., Messinger, J., Bergmann, U., Boal, A. K., Bollinger, J. M., Krebs, C., Högbom, M., Phillips, G. N., Vierstra, R. D., Sauter, N. K., Orville, A. M., Kern, J., Yachandra, V. K. & Yano, J. (2017). *Nat. Methods*, **14**, 443–449.

Grünbein, M. L., Bielecki, J., Gorel, A., Stricker, M., Bean, R., Cammarata, M., Dörner, K., Fröhlich, L., Hartmann, E., Hauf, S., Hilpert, M., Kim, Y., Kloos, M., Letrun, R., Messerschmidt, M., Mills, G., Nass Kovacs, G., Ramilli, M., Roome, C. M., Sato, T., Scholz, M., Sliwa, M., Sztuk-Dambietz, J., Weik, M., Weinhausen, B., Al-Qudami, N., Boukhelef, D., Brockhauser, S., Ehsan, W., Emons, M., Esenov, S., Fangohr, H., Kaukher, A., Kluyver, T., Lederer, M., Maia, L., Manetti, M., Michelat, T., Münnich, A., Pallas, F., Palmer, G., Previtali, G., Raab, N., Silenzi, A., Szuba, J., Venkatesan, S., Wrona, K., Zhu, J., Doak, R. B., Shoeman, R. L., Foucar, L., Colletier, J., Mancuso, A. P., Barends, T. R. M., Stan, C. A. & Schlichting, I. (2018). *Nat. Commun.* **9**, 3487.

Herrmann, S., Boutet, S., Duda, B., Fritz, D., Haller, G., Hart, P., Herbst, R., Kenney, C., Lemke, H., Messerschmidt, M., Pines, J., Robert, A., Sikorski, M. & Williams, G. (2013). *Nucl. Instrum. Methods Phys. Res. A*, **718**, 550–553.

Jacquamet, L., Traoré, D. A. K., Ferrer, J. L., Proux, O., Testemale, D., Hazemann, J. L., Nazarenko, E., El Ghazouani, A., Caux-Thang, C., Duarte, V. & Latour, J. M. (2009). *Mol. Microbiol.* **73**, 20–31.

Kachel, T., Pontius, N., Stamm, C., Wietstruk, M., Aziz, E. F., Dürr, H. A., Eberhardt, W. & de Groot, F. M. F. (2009). *Phys. Rev. B*, **80**, 092404.

Kroll, T., Kern, J., Kubin, M., Ratner, D., Gul, S., Fuller, F. D., Löchel, H., Krzywinski, J., Lutman, A., Ding, Y. T., Dakovski, G. L., Moeller, S., Turner, J. J., Alonso-Mori, R., Nordlund, D. L., Rehanek, J., Weniger, C., Firsov, A., Brzhezinskaya, M., Chatterjee, R., Lassalle-Kaiser, B., Sierra, R. G., Laksmono, H., Hill, E., Borovik, A., Erko, A., Föhlisch, A., Mitzner, R., Yachandra, V. K., Yano, J., Wernet, P. & Bergmann, U. (2016). *Opt. Express*, **24**, 22469–22480.

Lemke, H. T., Bressler, C., Chen, L. X., Fritz, D. M., Gaffney, K. J., Galler, A., Gawelda, W., Haldrup, K., Hartsock, R. W., Ihee, H., Kim, J., Kim, K. H., Lee, J. H., Nielsen, M. M., Stickrath, A. B., Zhang, W. K., Zhu, D. L. & Cammarata, M. (2013). *J. Phys. Chem. A*, **117**, 735–740.

Levantino, M., Schirò, G., Lemke, H. T., Cottone, G., Glownia, J. M., Zhu, D. L., Chollet, M., Ihee, H., Cupane, A. & Cammarata, M. (2015). *Nat. Commun.* **6**, 6772.
Levy, M., Ferrari, R., Franks, P. J. S., Martin, A. P. & Riviere, P. (2012). *Geophys. Res. Lett.* **39**, L14602.
Mara, M. W., Hadt, R. G., Reinhard, M. E., Kroll, T., Lim, H., Hartsock, R. W., Alonso-Mori, R., Chollet, M., Glownia, J. M., Nelson, S., Sokaras, D., Kunnus, K., Hodgson, K. O., Hedman, B., Bergmann, U., Gaffney, K. J. & Solomon, E. I. (2017). *Science*, **356**, 1276–1280.
Miller, N. A., Deb, A., Alonso-Mori, R., Garabato, B. D., Glownia, J. M., Kiefer, L. M., Koralek, J., Sikorski, M., Spears, K. G., Wiley, T. E., Zhu, D. L., Kozlowski, P. M., Kubarych, K. J., Penner-Hahn, J. E. & Sension, R. J. (2017). *J. Am. Chem. Soc.* **139**, 1894–1899.
Ratner, D., Abela, R., Amann, J., Behrens, C., Bohler, D., Bouchard, G., Bostedt, C., Boyes, M., Chow, K., Cocco, D., Decker, F. J., Ding, Y., Eckman, C., Emma, P., Fairley, D., Feng, Y., Field, C., Flechsig, U., Gassner, G., Hastings, J., Heimann, P., Huang, Z., Kelez, N., Krzywinski, J., Loos, H., Lutman, A., Marinelli, A., Marcus, G., Maxwell, T., Montanez, P., Moeller, S., Morton, D., Nuhn, H. D., Rodes, N., Schlotter, W., Serkez, S., Stevens, T., Turner, J., Walz, D., Welch, J. & Wu, J. (2015). *Phys. Rev. Lett.* **114**, 054801.
Ravel, B. & Newville, M. (2005). *J. Synchrotron Rad.* **12**, 537–541.
Rehr, J. J. & Albers, R. C. (2000). *Rev. Mod. Phys.* **72**, 621–654.
Sarangi, R., York, J. T., Helton, M. E., Fujisawa, K., Karlin, K. D., Tolman, W. B., Hodgson, K. O., Hedman, B. & Solomon, E. I. (2008). *J. Am. Chem. Soc.* **130**, 676–686.
Shelby, M. L., Lestrange, P. J., Jackson, N. E., Haldrup, K., Mara, M. W., Stickrath, A. B., Zhu, D. L., Lemke, H. T., Chollet, M., Hoffman, B. M., Li, X. S. & Chen, L. X. (2016). *J. Am. Chem. Soc.* **138**, 8752–8764.
Shelby, M. L., Mara, M. W. & Chen, L. X. (2014). *Coord. Chem. Rev.* **277–278**, 291–299.
Sierra, R. G., Gati, C., Laksmono, H., Dao, E. H., Gul, S., Fuller, F., Kern, J., Chatterjee, R., Ibrahim, M., Brewster, A. S., Young, I. D., Michels-Clark, T., Aquila, A., Liang, M., Hunter, M. S., Koglin, J. E., Boutet, S., Junco, E. A., Hayes, B., Bogan, M. J., Hampton, C. Y., Puglisi, E. V., Sauter, N. K., Stan, C. A., Zouni, A., Yano, J., Yachandra, V. K., Soltis, S. M., Puglisi, J. D. & DeMirci, H. (2016). *Nat. Methods*, **13**, 59–62.
Sierra, R. G., Laksmono, H., Kern, J., Tran, R., Hattne, J., Alonso-Mori, R., Lassalle-Kaiser, B., Glöckner, C., Hellmich, J., Schafer, D. W., Echols, N., Gildea, R. J., Grosse-Kunstleve, R. W., Sellberg, J., McQueen, T. A., Fry, A. R., Messerschmidt, M. M., Miahnahri, A., Seibert, M. M., Hampton, C. Y., Starodub, D., Loh, N. D., Sokaras, D., Weng, T.-C., Zwart, P. H., Glatzel, P., Milathianaki, D., White, W. E., Adams, P. D., Williams, G. J., Boutet, S., Zouni, A., Messinger, J., Sauter, N. K., Bergmann, U., Yano, J., Yachandra, V. K. & Bogan, M. J. (2012). *Acta Cryst.* D**68**, 1584–1587.
Smolentsev, G. & Soldatov, A. (2006). *J. Synchrotron Rad.* **13**, 19–29.
Tschentscher, T., Bressler, C., Grunert, J., Madsen, A., Mancuso, A. P., Meyer, M., Scherz, A., Sinn, H. & Zastrau, U. (2017). *Appl. Sci.* **7**, 592.
Wiedorn, M. O., Oberthür, D., Bean, R., Schubert, R., Werner, N., Abbey, B., Aepfelbacher, M., Adriano, L., Allahgholi, A., Al-Qudami, N., Andreasson, J., Aplin, S., Awel, S., Ayyer, K., Bajt, S., Barák, I., Bari, S., Bielecki, J., Botha, S., Boukhelef, D., Brehm, W., Brockhauser, S., Cheviakov, I., Coleman, M. A., Cruz-Mazo, F., Danilevski, C., Darmanin, C., Doak, R. B., Domaracky, M., Dörner, K., Du, Y., Fangohr, H., Fleckenstein, H., Frank, M., Fromme, P., Gañán-Calvo, A. M., Gevorkov, Y., Giewekemeyer, K., Ginn, H. M., Graafsma, H., Graceffa, R., Greiffenberg, D., Gumprecht, L., Göttlicher, P., Hajdu, J., Hauf, S., Heymann, M., Holmes, S., Horke, D. A., Hunter, M. S., Imlau, S., Kaukher, A., Kim, Y., Klyuev, A., Knoška, J., Kobe, B., Kuhn, M., Kupitz, C., Küpper, J., Lahey-Rudolph, J. M., Laurus, T., Le Cong, K., Letrun, R., Xavier, P. L., Maia, L., Maia, F. R. N. C., Mariani, V., Messerschmidt, M., Metz, M., Mezza, D., Michelat, T., Mills, G., Monteiro, D. C. F., Morgan, A., Mühlig, K., Munke, A., Münnich, A., Nette, J., Nugent, K. A., Nuguid, T., Orville, A. M., Pandey, S., Pena, G., Villanueva-Perez, P., Poehlsen, J., Previtali, G., Redecke, L., Riekehr, W. M., Rohde, H., Round, A., Safenreiter, T., Sarrou, I., Sato, T., Schmidt, M., Schmitt, B., Schönherr, R., Schulz, J., Sellberg, J. A., Seibert, M. M., Seuring, C., Shelby, M. L., Shoeman, R. L., Sikorski, M., Silenzi, A., Stan, C. A., Shi, X., Stern, S., Sztuk-Dambietz, J., Szuba, J., Tolstikova, A., Trebbin, M., Trunk, U., Vagovic, P., Ve, T., Weinhausen, B., White, T. A., Wrona, K., Xu, C., Yefanov, O., Zatsepin, N., Zhang, J., Perbandt, M., Mancuso, A. P., Betzel, C., Chapman, H. & Barty, A. (2018). *Nat. Commun.* **9**, 4025.